Nanoscale

PAPER

View Article Online
View Journal | View Issue

Cite this: *Nanoscale*, 2018, **10**, 21483

Rattle-type porous Sn/C composite fibers with uniformly distributed nanovoids containing metallic Sn nanoparticles for high-performance anode materials in lithium-ion batteries†

Ju Ho Lee,‡[a] Se Hwan Oh,‡[a] Sun Young Jeong,[a] Yun Chan Kang *[b] and Jung Sang Cho *[a]

Received 28th July 2018,
Accepted 22nd October 2018

DOI: 10.1039/c8nr06075d

rsc.li/nanoscale

Rattle-type porous Sn/carbon (Sn/C) composite fibers with uniformly distributed nanovoids containing metallic Sn nanoparticles in void space surrounded by C walls (denoted as RT-Sn@C porous fiber) were prepared by electrospinning and subsequent facile heat-treatment. Highly concentrated polystyrene nanobeads used as a sacrificial template played a key role in the synthesis of the unique structured RT-Sn@C porous fiber. The RT-Sn@C porous fiber exhibited excellent long-term cycling and rate performances. The discharge capacity of the RT-Sn@C porous fiber at the 1000th cycle was 675 mA h g^{-1} at a high current density of 3.0 A g^{-1}. The RT-Sn@C porous fiber had final discharge capacities of 991, 924, 890, 848, 784, 717, 679, and 614 mA h g^{-1} at current densities of 0.1, 0.2, 0.3, 0.5, 1.0, 2.0, 3.0, 5.0, and 10.0 A g^{-1}, respectively. The numerous void spaces, surrounding a Sn nanoparticle as the rattle-type particle, and the surrounding C could efficiently accommodate the volume changes of the Sn nanoparticles, improve the electrical conductivity, and enable efficient penetration of the liquid electrolyte into the structure.

Introduction

In recent times, rechargeable lithium ion batteries (LIBs) with high energy and power density, and long cycle lifetime have been attracting significant attention in the fields of electric vehicles (EV) and energy storage systems (ESS).[1–10] Elements such as silicon (Si), tin (Sn), and germanium (Ge) which are capable of alloying with Li^+ ions have been thoroughly researched as alternatives to conventional graphite anode materials owing to their very high theoretical capacities.[11–15] Among them, metallic Sn, as $Li_{4.4}Sn$, is considered to be one of the next generation anode materials for LIBs due to its high theoretical capacity of 992 mA h g^{-1}, high electrical conductivity, and moderate operating voltage for the safety of LIBs during the repeated lithiation/delithiation process.[16–18] However, practical implementation of metallic Sn to LIBs is hampered by the huge volume change of 260% and aggregation of Sn particles during cycling, which induces a very rapid capacity decay and poor cyclability.[19,20]

To overcome these challenges, numerous efforts have been devoted to designing suitable Sn anodes for LIBs, which generally include reducing the Sn particle size, compositing with carbon, and containing enough void volume to accommodate the stress associated with the large volume change of Sn.[21–30] For example, Yu *et al.*[26] prepared Sn@C nanoparticles encapsulated in bamboo-like hollow carbon fibers, by coaxial electrospinning. They exhibited a high capacity of 737 mA h g^{-1} after 200 cycles at 0.5 C. Also, Qin *et al.*[27] fabricated 3D porous graphene networks anchored with Sn nanoparticles encapsulated with graphene shells by a chemical vapor deposition process. As a result, long-term cycling stability at high rates (a high capacity of 682 mA h g^{-1} was achieved at 2.0 A g^{-1} after 1000 cycles) and superior rate capability (270 mA h g^{-1} at 10 C) were achieved. Huang *et al.*[28] reported a hierarchical Sn/C composite in which some of the nanosized Sn particles are anchored to the tips of carbon nanotubes that are rooted on the exterior surfaces of micro-sized hollow carbon cubes, while other Sn nanoparticles are encapsulated in hollow carbon cubes. It delivered a capacity of 786 mA h g^{-1} at 600 mA g^{-1} for 200 cycles. The Sn/C composite anodes reported to date have

[a]*Department of Engineering Chemistry, Chungbuk National University, Chungbuk 361-763, Republic of Korea. E-mail: jscho@cbnu.ac.kr; Fax: (+82) 43-262-2380*
[b]*Department of Materials Science and Engineering, Korea University, Anam-Dong, Seongbuk-Gu Seoul 136-713, Republic of Korea. E-mail: yckang@korea.ac.kr; Fax: (+82) 2-928-3584*

†Electronic supplementary information (ESI) available. See DOI: 10.1039/c8nr06075d

‡These authors contributed equally to the work.

been designed to preserve the structural and interfacial stabilization of the Sn nanoparticles during cycling, resulting in an improved cycling performance.[29,30] However, a new strategy and more rational design of Sn anodes for practical implementation are necessary which will require controlling both the size of the Sn particle and the void volume and their configuration in the C matrix.

In this study, we have achieved for the first time the unique Sn/C composite fibers with uniformly distributed nanovoids containing one metallic Sn nanoparticle, as a rattle-type structure by electrospinning and a subsequent facile reduction process. The size-controlled polystyrene (PS) nanobeads in the spinning solution after decomposition enable precise control of the void size and uniform distribution of nanovoids in the composite nanostructure. Therefore, efficiently reducing the amount of gas diffused into the structure through the void pathway during heat-treatment induces formation of uniform sized metallic Sn nanoparticles spread evenly all over the C matrix. Subsequently, by tuning the ramping rate during heat-treatment each void space surrounded by carbon walls was taken up by a Sn nanoparticle making the structure a rattle-type structure. To the best of our knowledge, the structure prepared in this study exhibited the best reversible capacity (at extremely high current densities with long cycle lifetime and excellent rate capability) ever reported in Sn based anodes with various morphologies. The formation mechanism of the unique Sn/C composite fibers with uniformly distributed nanovoids, containing a metallic Sn nanoparticle, was investigated, and their Li^+ ion storage properties as anode materials were studied in detail.

Experimental

Sample preparation

Porous Sn/C composite fibers with uniformly distributed nanovoids, containing a metallic Sn nanoparticle, were prepared by electrospinning and subsequent heat-treatment. First, the precursor fibers composed of Sn salt, polyvinyl alcohol, and PS nanobeads were prepared by electrospinning. Size-controlled PS nanobeads with a diameter of 140 nm were synthesized by an emulsifier-free emulsion polymerization method. The spinning solution was prepared by dissolving 2.0 g of tin(IV) chloride pentahydrate ($SnCl_4{\cdot}5H_2O$, Kanto, 98.0%) and 1.5 g of polyvinyl alcohol (PVA 2000, Kanto) in 15 mL ethyl alcohol (EtOH, Duksan, 99.9%). Then, 15 mL aqueous suspension containing PS nanobeads (1.5 g) as a void creator was added to the above solution and it was stirred overnight vigorously. The prepared spinning solution was loaded into a plastic syringe equipped with a 23-gauge stainless steel nozzle, ejected at a flow rate of 1 mL h^{-1}, and electrospun onto a drum collector. During electrospinning, the distance between the tip and the collector was maintained at 12 cm, while the rotation speed of the drum was maintained at 150 rpm. A voltage of 20 kV was applied between the collector and the syringe tip. The resulting as-spun fibers composed of Sn salt, PVA, and PS nanobeads were stabilized at 100 °C in air for 24 h. Subsequently, the composite fibers were thermally treated at 400 °C at a ramping rate of 1 °C min^{-1} for 1 min under a H_2/Ar reducing atmosphere. This resulted in the synthesis of rattle-type (RT) porous Sn/C composite fibers, with uniformly distributed nanovoids that contain one metallic Sn nanoparticle; these fibers are henceforth denoted as "RT-Sn@C porous fiber". The composite with carbon fibers and separated Sn nanoparticles which are obtained after heat-treatment of Sn salt/PVA composite fibers without PS nanobeads is denoted as "Sn/C fiber".

Characterization techniques

The crystal structure of the tin fibers was investigated by X-ray diffraction (XRD, Bruker AXS, D8 Discover with GADDS). The morphologies were observed using field-emission scanning electron microscopy (FE-SEM, Zeiss, ULTRA Plus) and high-resolution transmission electron microscopy (HR-TEM, JEOL, JEM-2100F) at a working voltage of 200 kV. X-ray photoelectron spectroscopy (XPS, Ulvac-PHI, PHI Quantera-II) was performed on the samples with Al Kα radiation (1486.6 eV). To determine the carbon content of the tin fibers, thermogravimetric analysis (TGA, TA Instruments Q600, PH407, KBSI BUSAN) was performed in air at a heating rate of 10 °C min^{-1}. The surface areas of the microspheres were determined by the Brunauer–Emmett–Teller (BET) method, with N_2 as the adsorbate gas (TriStar 3000 gas adsorption analyzer, Micromeritics, USA).

Electrochemical measurements

The electrochemical properties of the tin fibers were analyzed by constructing a 2032-type coin cell. The anode was prepared by mixing the active material, carbon black, and sodium carboxymethyl cellulose (CMC) in a weight ratio of 7 : 2 : 1. The Li metal and a microporous polypropylene film were used as the counter electrode and the separator, respectively. The electrolyte was 1 M $LiPF_6$ in a 1 : 1 (v/v) mixture of fluoroethylene carbonate and dimethyl carbonate (FEC–DMC). The charge/discharge characteristics of the samples were investigated by cycling over a potential range of 0.001 to 3.0 V at various current densities. Cyclic voltammograms (CVs) recorded at a scan rate of 0.01 mV s^{-1} were examined. The size of the negative electrode containing the tin fibers was 1.4 cm × 1.4 cm and the mass loading was approximately 0.91 mg cm^{-2}. In this study, the capacities of the samples were calculated based on the total mass of the prepared sample. Electrochemical impedance spectra were obtained by performing alternating-current electrochemical impedance spectroscopy (EIS, ZIVE SP1) over a frequency range of 0.01 Hz to 100 kHz at 1 mV potential. For the full cell assembly, commercial $LiCoO_2$ powders were used as the positive electrode and the loading mass was 6.7 mg cm^{-2}, whereas the anode mass loading was kept at 0.91 mg cm^{-2}. Before fabrication of the full-cell with the $LiCoO_2$ cathode, the RT-Sn@C porous fiber electrode was prelithiated to decrease the ICL (irreversible capacity loss) by several cycles of the half-cell assembly between 0.001 and 3.0 V. For the full-cell test, 1 M $LiPF_6$ dissolved in a mixture of ethylene carbonate/diethyl carbonate (EC/DEC; 1 : 1 v/v) was used as the electrolyte. The electrochemical properties of the

2032-type coin full-cells were examined at 0.2 A g^{-1} in the voltage window of 1.2–4.2 V. The electrode capacity was calculated relative to the weight of the anode materials.

Results and discussion

Rattle-type porous Sn/C composite fibers, with uniformly distributed nanovoids containing one metallic Sn nanoparticle and surrounded by carbon walls, (denoted as RT-Sn@C porous fiber) were prepared by the electrospinning process and subsequent facile heat-treatment. The formation mechanism of the unique RT-Sn@C porous fiber structure is described in Scheme 1a. Electrospinning was performed on an aqueous spinning solution containing size-controlled PS nanobeads of 140 nm, Sn salt, polyvinyl alcohol (PVA), and ethyl alcohol (EtOH). By adding size-controlled PS nanobeads in the form of an aqueous suspension, precise control of the void size and uniform distribution of nanovoids in the as-spun fibers was possible. After the spinning process, the precursor fiber composed of Sn salt and PVA containing uniformly dispersed PS nanobeads was obtained. During the simple heat-treatment, PVA was first carbonized (decomposition temp. ≈ 250 °C (ref. 31)) and subsequently PS nanobeads were decomposed into gaseous products (decomposition temp. ≈ 300 °C (ref. 32)); thereafter, the porous C matrix containing numerous uniformly distributed spherical nanovoids was prepared. In addition, Sn salts were reduced to metallic Sn nuclei and agglomerated into spherical metallic Sn nanoparticles. The reducing gas could efficiently diffuse into the fiber structure through the interconnected void pathway formed by the PS decomposition. This prevented the separation of Sn nanoparticles from the C fiber due to the Ostwald ripening effect. As a result, metallic Sn nanospheres with an average size of 40 nm were included in each void space formed by the decomposition of PS beads after heat-treatment. In this process, the ramping rate affected the final geometry of the Sn/C composite fibers significantly. At a low ramping rate of 1 °C min^{-1}, a Sn salt/PVA composite fiber was almost homogeneously heated from the surface to the center owing to the minimization of the temperature gradient, which enabled the formation of uniformly distributed Sn nanoparticles with a narrow size distribution, and encapsulated in the void space as a rattle type without being exposed to the fiber surface. Therefore, porous Sn/C composite fibers with uniformly distributed nanovoids that contain metallic Sn nanoparticles in the void spaces were prepared by electrospinning and subsequent heat-treatment, as described in Scheme 1a. It is noteworthy that the synthesis of the unique RT-Sn@C porous fiber structure was possible with the help of both the ramping rate control and the porous structure during heat-treatment by preventing the Ostwald ripening effect. However, Ostwald ripening of Sn could not be prevented effectively for a high ramping rate of 10 °C min^{-1} and for a filled structure during heat-treatment. Therefore, the Sn particles separated from the carbon fibers were obtained as shown in Scheme 1b and c.

The formation mechanism of the RT-Sn@C porous fiber was investigated in detail by tracing both the fiber morphology and phase at each step. As is seen from Fig. 1a, the as-spun fiber exhibited a uniform diameter of 1.0 μm and a bumpy fiber surface as shown in the inset image. This confirms that the PS nanobeads of 140 nm (Fig. S1†) were uniformly contained in the as-spun fiber structure. Addition of PS nanobeads in the form of an aqueous suspension ensured that no agglomeration of the PS nanobeads was locally possible in the structure. XRD analysis confirmed low crystalline peaks related to $SnCl_4$, PVA, and PS as shown in Fig. 1b.

The rattle-type porous Sn/C composite fibers with uniformly distributed nanovoids containing one metallic Sn nanoparticle

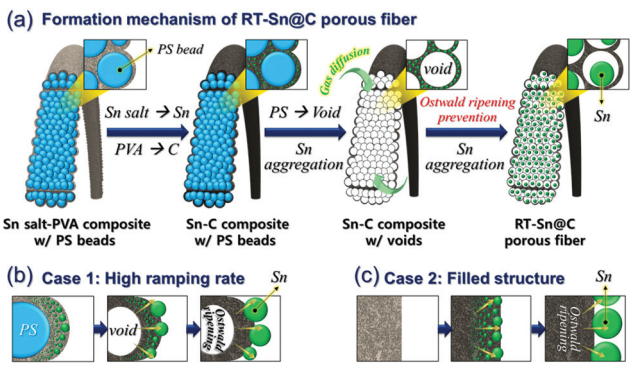

Scheme 1 Formation mechanisms of (a) RT-Sn@C porous fibers, (b) porous C fibers with separated Sn particles, and (c) filled C fibers with separated Sn particles.

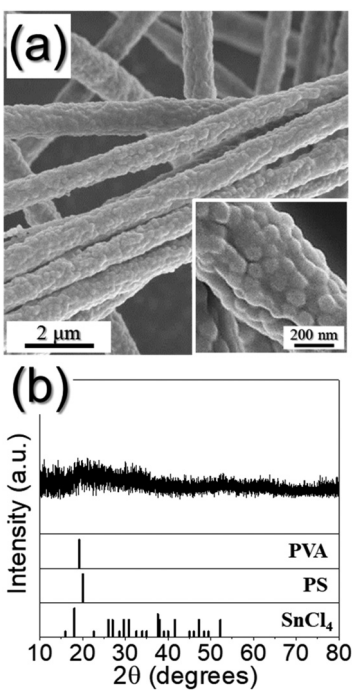

Fig. 1 (a) FE-SEM images and (b) XRD pattern of the as-spun Sn salt/PVA composite fibers containing PS nanobeads prepared by electrospinning.

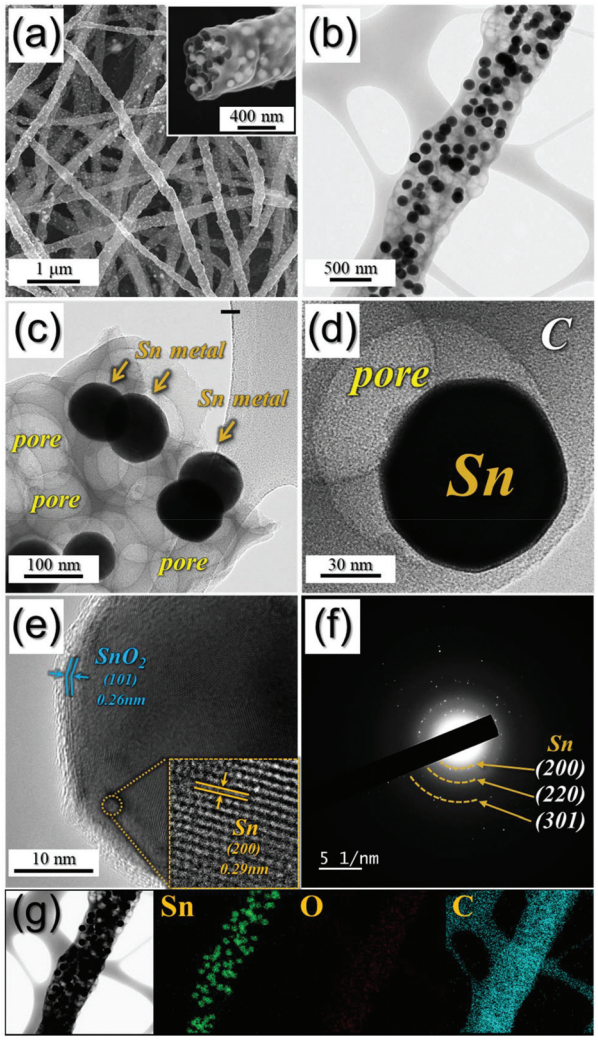

Fig. 2 Morphologies, SAED pattern, and elemental mapping images of the RT-Sn@C porous fiber obtained after heat-treatment of as-spun Sn salt/PVA composite fibers containing PS nanobeads at 400 °C at a ramping rate of 1 °C min^{-1} under 10% H_2/Ar gas for 1 min: (a) FE-SEM images, (b and c) TEM images, (d and e) HR-TEM images, (f) SAED pattern, and (g) elemental mapping images.

were obtained after a heat-treatment of the as-spun fibers under a reducing atmosphere as shown in Fig. 2. Phase analysis in Fig. S2† reveals Sn salt reduction. Therefore, pure metallic Sn, in the absence of any crystalline tin-oxides, was slowly formed in the structure during the temperature increase to 400 °C. In this process complete decomposition of the PS nanobeads, carbonization of PVA, and subsequent thermal contraction of carbon generated the porous C matrix including nanovoids with an average diameter of 100 nm all over the nanostructure as shown in Fig. 2a–d. It is noteworthy that the reducing gas diffused efficiently into the SnO_x/C composite structure during heat-treatment through the numerous nanovoid pathways. This enabled the formation of uniformly distributed Sn nanoparticles, with a narrow size distribution, all over the porous C matrix without being exposed to the fiber surface. This indicates that the Sn nanoparticles with an average diameter of 50 nm were contained in the void spaces enclosed by the C matrix as a rattle-type as shown in Fig. 2c and d. The Sn nanoparticles inside of the nanovoids were further confirmed in Fig. S3.† The void space surrounding the Sn nanoparticle and the surrounding C matrix can efficiently accommodate the huge volume changes (about 260%) of the Sn nanoparticles during the lithiation/delithiation process, thus increasing the structural stability. Moreover, the electrolyte could be penetrated into the structure through the interconnected void channels formed by PS decomposition thus increasing the rate property of the composite. The high-resolution TEM images of the Sn nanoparticle in the RT-Sn@C porous fiber are shown in Fig. 2e. The clear lattice fringes separated by 0.29 nm, which correspond to the (200) crystal plane of the metallic Sn phase, were confirmed.[33] In addition, the SnO_2 phase with the (101) plane on the surface due to the partial oxidation of Sn was observed when exposed to air.[34] The selected area electron diffraction (SAED) pattern in Fig. 2f confirmed the formation of the metallic Sn nanospheres in the C matrix, which agrees well with the above XRD result. The elemental mapping images shown in Fig. 2g further emphasized the uniform distribution of the metallic Sn nanoparticles throughout the porous carbon fibers with numerous nanovoids.

In this study, it was possible to incorporate metallic Sn nanoparticles uniformly into the void spaces surrounded by carbon to form a rattle-type structure owing to both the porous structure and ramping rate control during the heat-treatment. These two factors affecting the fiber morphology are demonstrated in detail in Fig. 3. The Sn salt/PVA composite electrospun from a solution without PS nanobeads is shown in Fig. S4.† It showed a smooth and filled fiber surface without any bumpy structure because there was no PS nanobead within the structure. Although the heat-treatment of the as-spun fibers was performed at a slow ramping rate of 1 °C min^{-1}, the reducing gas could not penetrate effectively into the filled Sn salt/PVA composite structure due to the absence of a channel pathway of interconnected voids. Therefore, metallic Sn nuclei (XRD in Fig. S5†) were preferentially formed at the fiber surface, which is easy to contact with the reducing gas, followed by Ostwald ripening, resulting in the local grain-growth of Sn particles. As a result, relatively larger Sn particles with a mean size of 450 nm separated from the C fibers were obtained after heat-treatment as shown in Fig. 3a and b. The ramping rate was also an important factor in obtaining the unique RT-Sn@C porous fiber structure during the heat-treatment. At a high ramping rate of 10 °C min^{-1}, the porous Sn salt/PVA composite fiber was heterogeneously heated owing to the maximization of the temperature gradient. Therefore, Sn nanoparticles were nucleated near the fiber surface and grew larger locally even though inward penetration of the reducing gas occurred efficiently through numerous nanovoids in the structure. As a result, the Sn particles separated from the porous C fibers were obtained, as shown in Fig. 3c and d similar to those by the filled Sn-salt/PVA composite fibers (Fig. 3a and b). In both the cases, the exposed Sn

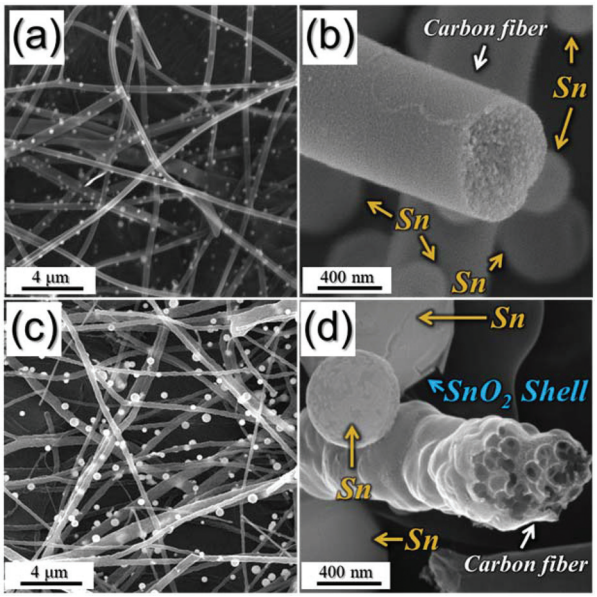

Fig. 3 Morphologies of (a and b) Sn/C composite fibers after heat-treatment of the as-spun Sn salt/PVA composite fibers without PS nanobeads at 400 °C under 5% H_2/Ar at a slow ramping rate of 1 °C min^{-1} and (c and d) Sn/C composite fibers after heat-treatment of the as-spun Sn salt/PVA composite fibers with PS nanobeads at 400 °C under 5% H_2/Ar at a high ramping rate of 10 °C min^{-1}.

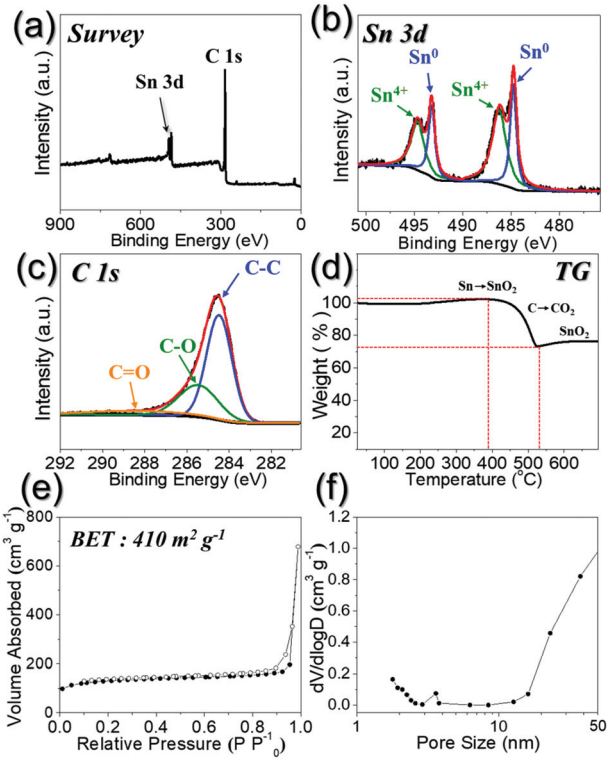

Fig. 4 Characteristics of RT-Sn@C porous fibers: (a) XPS survey spectrum, (b) XPS Sn 3d spectrum, (c) XPS C 1s spectrum, (d) TG curve, (e) N_2 adsorption–desorption isotherms, and (f) pore size distribution.

particles that had separated from the C fiber were oxidized to some extent on the surface; therefore, the SnO_2 shell was observed as indicated by the arrow in Fig. 3d.

The characteristics of the resulting RT-Sn@C porous fiber prepared by adapting the porous structure and optimum ramping rate during heat-treatment are shown in Fig. 4. The chemical information of the RT-Sn@C porous fiber was investigated by analyzing the XPS spectrum shown in Fig. 4a–c. The XPS survey spectrum reveals that the RT-Sn@C porous fiber contained metallic Sn and C elements (Fig. 4a). The Sn 3d spectra in Fig. 4b show Sn $3d_{3/2}$ and $3d_{5/2}$ peaks at 484.8 and 493.21 eV, respectively, confirming the formation of the metallic Sn phase.[35,36] In addition, the peaks at 486.24 eV (Sn $3d_{5/2}$) and 494.62 eV (Sn $3d_{3/2}$) related to the tin oxide were observed owing to the partial surface oxidation of the Sn nanoparticles in the sample which commonly occurs under ambient conditions. However, since numerous Sn nanoparticles in the voids were surrounded by the C matrix, Sn oxidation could be prevented to some extent. Fig. 4c shows the C 1s XPS spectrum of the RT-Sn@C porous fiber, in which peaks corresponding to sp^2-bonded carbon (C–C), epoxy and alkoxy groups (C–O), and carbonyl and carboxylic (C═O) components were observed at 284.5, 285.5, and 288.4 eV, respectively.[37]

The TG curve of the RT-Sn@C porous fiber is shown in Fig. 4d. The initial weight increase observed between 200 and 400 °C was attributed to the oxidation of the Sn metal. Subsequently, a critical weight loss above 450 °C was observed due to the combustion of the C matrix. The weight loss was diminished by the continuous Sn oxidation process (Sn → SnO → SnO_2). The carbon content in the RT-Sn@C porous fiber as calculated from the TGA and elemental analysis (Table S1†) results was 35 wt%.

The nitrogen adsorption/desorption isotherms and Barrett–Joyner–Halenda (BJH) pore size distributions of the RT-Sn@C porous fiber are shown in Fig. 4e and f, respectively. The isotherms exhibited that micropores under 2 nm diameter originated due to both the carbonization of PVP and Sn nuclei migration to form Sn nanoparticles in the C matrix and mesopores below 50 nm diameter, attributed to the space between the nanovoids, formed due to the PS nanobead decomposition. The Sn metal as a rattle-type was contained within the RT-Sn@C porous fiber as seen in Fig. 4f. In addition, mesopores of approximately 3.5 nm diameter were attributed to the tensile strength of the fiber; the effect of nitrogen desorption was also confirmed.[38] The Brunauer–Emmett–Teller (BET) surface area of the RT-Sn@C porous fiber was 410 m^2 g^{-1}. The high BET value is caused by the presence of micropores in the amorphous C matrix of the RT-Sn@C porous fiber.

The effects of morphological features of the RT-Sn@C porous fiber on electrochemical properties were compared with those of the composite with C fibers and separated metallic Sn nanoparticles (Sn/C fiber) prepared by heat-treatment of the filled Sn-salt/PVA composite fibers as shown in Fig. 3a and b. Fig. 5a shows the CV curves of the RT-Sn@C porous fiber during the initial 5 cycles at a scan rate of 0.1 mV s^{-1} in

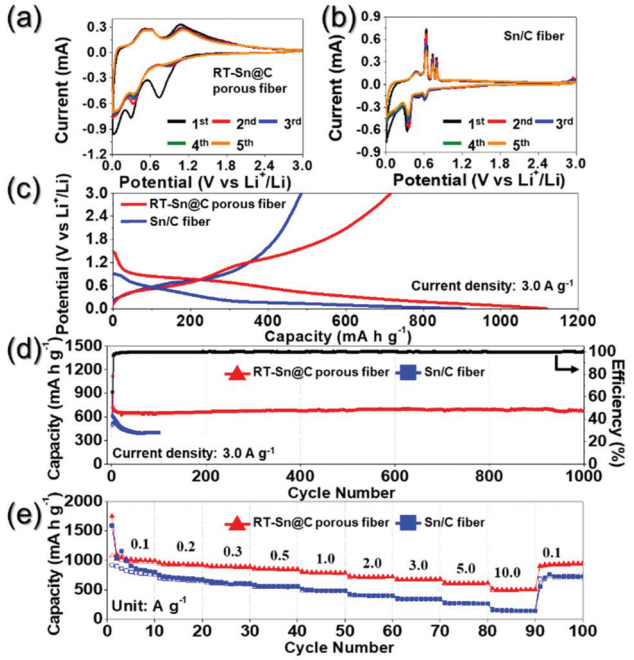

Fig. 5 CV curves of (a) RT-Sn@C porous fibers and (b) Sn/C fiber scanned at a rate of 0.1 mV s^{-1}, (c) initial discharge–charge profiles, (d) cycling performances at a current density of 3.0 A g^{-1}, and (e) rate performances.

the potential range 0.001–3.0 V. In the first cathodic scan, the irreversible peak for the decomposition of the electrolyte to form a solid electrolyte interphase (SEI) layer and lithium alloying with Sn were confirmed at 0.72 V. A reduction peak at 0.36 V is assigned to the further lithiation of Sn to form a series of Li_xSn alloys.[39–43] Subsequently, the Li^+ ion insertion into the amorphous C matrix was observed at 0.12 V.[44,45] During the anodic scans, the broad oxidation peak near 0.6 V was attributed to the delithiation reaction of the Li_xSn alloy.[39–43] The subsequent broad peak at 1.2 V was attributed to the lithium extraction from the C matrix.[44,45] The good overlapping of the CV curves from the second cycle onward confirmed good cycling stability of the electrochemical reactions during the first 5 cycles.[39–43] CV curves of the Sn/C fiber in Fig. 5b show relatively sharp reduction peaks at 0.34, 0.52, and 0.61 V corresponding to lithium alloying with tin forming Li_xSn alloys.[39–43] The peak for the formation of the SEI layer in the Sn/C composite fibers was also observed at 0.62 V. In the anodic scan, sharp reaction peaks at 0.46, 0.63, 0.74, and 0.79 V corresponding to transition from $Li_{22}Sn_5$ to Li_7Sn_3, LiSn, Li_2Sn_5, and Sn, respectively, were observed.[39–43] In addition, an abnormal peak at 2.95 V was also detected in the first anodic scan, which is attributed to the presence of oxygen in the anodes.[39–43] In the Sn/C fiber sample, exposed Sn particles from the C fiber were oxidized and they formed the SnO_2 shells. The different morphological features of the two Sn–C composites changed the shapes of the CV traces.

RT-Sn@C porous fibers show a relatively broad CV curve, which is attributed to the nano-sized Sn particles in the structure. Although RT-Sn@C porous fibers also undergo electrochemical reactions in multiple steps during the cycling, the several peaks for lithiation/delithiation are superimposed, which results in a broad CV peak.

The initial discharge and charge curves of the samples at a high current density of 3.0 A g^{-1} are shown in Fig. 5c. The RT-Sn@C porous fiber and Sn/C fiber exhibited the initial discharge capacities of 1118 and 907 mA h g^{-1}, respectively, and their initial coulombic efficiencies (CE) were 62 and 53%, respectively. The lower initial CE of the Sn/C fiber may be attributed to the higher C content of 53 wt% (Table S1†) with high initial irreversible capacity loss (ICL).[46] The carbonization efficiency of PVA was higher in the filled Sn salt-PVA composite structure than that in the porous structure with voids during heat-treatment at 400 °C. In addition, the structural destruction and formation of the SEI layer associated with the electrolyte decomposition, which is an irreversible process, may have resulted in the low initial CE of the Sn/C fiber.[46]

The cycling performances of the samples at a constant high current density of 3.0 A g^{-1} are also shown in Fig. 5d. The Sn/C fiber showed very fast capacity fading during the cycles; the discharge capacity after the 100th cycle was 398 mA h g^{-1}. This is due to the structural destruction and aggregation of the exposed Sn nanoparticles during cycling. In this study, the ramping rate was also an important factor to achieve the unique RT-Sn@C porous fiber structure during the heat-treatment. The Sn/C composite nanofibers prepared at a high ramping rate of 10 °C min^{-1} also showed poor cycle properties, as shown in Fig. S6.† On the other hand, the discharge capacity of the RT-Sn@C porous fiber decreased only slightly from 718 to 646 mA h g^{-1} during the first 100 cycles from the second cycle which is due to the slight pulverization of the Sn nanoparticle inside the void space. However, the C matrix surrounding Sn@void could effectively buffer the volume expansion of the Sn nanoparticles. In addition, the Sn nanoparticle contained in the void space as a rattle-type could restrain the aggregation of Sn nanoparticles thus maintaining the structural stability. Therefore, the RT-Sn@C porous fiber showed an excellent long-term cycle property during 1000 cycles even at an extremely high current density of 3.0 A g^{-1}. The discharge capacity of the RT-Sn@C porous fiber at the 1000th cycle was 675 mA h g^{-1} and its capacity retention measured from the second cycle was 94%. In addition, coulombic efficiency was steadily maintained at over 99%, which proves the efficient transport of Li^+ ions and electrons in the structure during cycling. The numerous void spaces surrounding a Sn nanoparticle as a rattle-type and the surrounding C could accommodate the volume changes of the Sn nanoparticles during the lithiation/delithiation process efficiently thus increasing the structural stability which enabled the superior cycle property of the RT-Sn@C porous fiber. In order to calculate the capacity contribution of the C matrix to the composite, the RT-Sn@C porous fiber was etched with HCl solution to obtain pure C fibers. From the EDS and CV measurement in Fig. S7† the complete removal of Sn in the structure was confirmed. The resulting porous C fibers are shown in Fig. S8a.† The first

discharge–charge profile confirms the fibers to be pure C fibers with discharge/charge capacities of 1349 and 541 mA h g^{-1}, respectively as shown in Fig. S8b.† The pure C fibers exhibited a reversible discharge capacity of 412 mA h g^{-1} at a current density of 3.0 A g^{-1} for the 200th cycle as shown in Fig. S8c.† Therefore, the contribution of the C matrix to the discharge capacity of the RT-Sn@C porous fiber could be estimated to be 20%. The C element with high initial ICL lowered the initial CE of the RT-Sn@C porous fiber. Fig. 5e shows the rate performances of the RT-Sn@C porous fiber and Sn/C fiber when the current density was increased stepwise from 0.1 to 10.0 A g^{-1}. The discharge capacity of the Sn/C fiber rapidly decreased from 795 to 263 mA h g^{-1} when the current density was increased from 0.1 to 10.0 A g^{-1}. On the other hand, the RT-Sn@C porous fiber exhibited an excellent rate performance even at high current densities. It is attributed to the synergetic effects of the C matrix and porous structure; the C matrix improved the electrical conductivity significantly and the porous structure enabled efficient penetration of the liquid electrolyte into the structure, thus shortening the diffusion path of the Li^+ ions. The RT-Sn@C porous fiber had final discharge capacities of 991, 924, 890, 848, 784, 717, 679, and 614 mA h g^{-1} at current densities of 0.1, 0.2, 0.3, 0.5, 1.0, 2.0, 3.0, 5.0, and 10.0 A g^{-1}, respectively. Subsequently, the capacities recovered well to 945 mA h g^{-1} when the current density was returned to 0.1 A g^{-1}, indicating that the RT-Sn@C porous fiber remained very stable even after cycling at high current densities. In this study, the excellent cycle, rate properties, and high reversible specific capacities were achieved which were better than any previously reported values of Sn based anodes with various morphologies (summarized in Table S2†).

The excellent electrochemical performances of the RT-Sn@C porous fiber were verified using electrochemical impedance spectroscopy (EIS) measurements before cycling and after 1 and 100 cycles, as shown in Fig. 6. The EIS spectra show semicircles in the medium frequency region and straight lines in the low frequency region, which correspond to the charge transfer resistance (R_{ct}) and the Warburg resistance of the two electrodes, respectively.[47–50] Nyquist plots were obtained by deconvolution with a Randle-type equivalent circuit model as shown in Fig. S9.† The electrochemical reaction types such as the charge transfer reaction, lithium ion migration through SEI layers, and Li^+ ion diffusion kinetics in the active materials are described by the equivalent circuit model. The RT-Sn@C porous fiber exhibited a lower R_{ct} value of 43 Ω than that of the Sn/C fiber (221 Ω) before cycling as shown in Fig. 6a. The uniform distribution of Sn nanoparticles in the C matrix with high electrical conductivity lowered the charge transfer resistance of the RT-Sn@C porous fiber. The R_{ct} values of the two electrodes were reduced to 11 and 18 Ω in the case of RT-Sn@C porous fiber and Sn/C fiber, respectively, after the 1st cycle; this occurred due to the transformation of the Sn crystals into ultrafine nanocrystals during initial cycling as shown in Fig. 6b. The low R_{ct} values of the RT-Sn@C porous fiber were well maintained even after repeated lithium alloying and dealloying reactions, while the Sn/C fiber showed increased charge transfer resistance as shown in Fig. 6c. The high structural stability of RT-Sn@C porous fiber during the repeated Li^+ ion charge and discharge processes resulted in the low R_{ct} values during cycling. The relationship between Z', the real part of the impedance spectra and $\omega^{-1/2}$ where ω is the angular frequency, in the low-frequency region after 100 cycles is shown in Fig. 6d. The slope of the curve for the RT-Sn@C porous fiber after the 100th cycle was significantly lower than that of the Sn/C fiber, which reveals the high Li^+ ion diffusion rate of the RT-Sn@C porous fiber. The morphologies of the RT-Sn@C porous fiber and Sn/C fiber obtained after 100 cycles for Li^+ ion storage are shown in Fig. 7 and Fig. S10,† respectively. The porous nanostructure of the RT-Sn@C porous fiber was well maintained even after repeated lithium alloying and dealloying reactions as shown in Fig. 7. The C matrix surrounding Sn@void could effectively buffer the volume expansion of Sn nanoparticles during cycling. However, the exposed Sn particles of the Sn/C fiber were broken into several pieces and aggregated after repeated cycles as observed in Fig. S10.† To confirm the possibility of the RT-Sn@C porous fiber for commercial application, the anode was pre-lithiated and combined with a commercial $LiCoO_2$ cathode to construct a full Li^+ ion cell. The $LiCoO_2$ active materials showed irregular powder morphology and a pure $LiCoO_2$ phase as shown in Fig. S11a and S11b.† The typical discharge–charge profile of $LiCoO_2$ in a half-cell and its cycle performance at a current density of 0.2 A g^{-1} are shown in Fig. S11c and S11d.† The charge/discharge curves and cycling performance of RT-Sn@C porous fiber/$LiCoO_2$ powder full-cells with a cut-off voltage in the range of 1.2–4.2 V are shown in Fig. 8. As shown in Fig. 8a, these

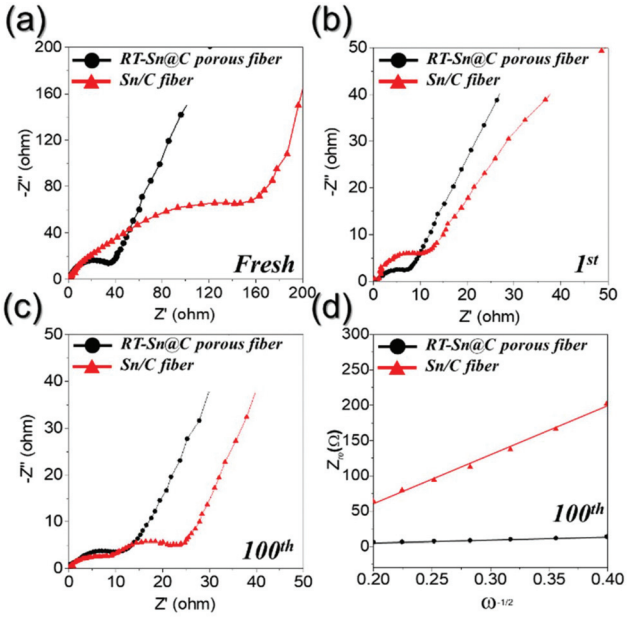

Fig. 6 (a–c) Nyquist impedance plots and (d) linear fits in the low-frequency region of RT-Sn@C porous fibers and Sn/C fiber: (a) before cycling, (b) after 1st cycling, and (c and d) after 100th cycling.

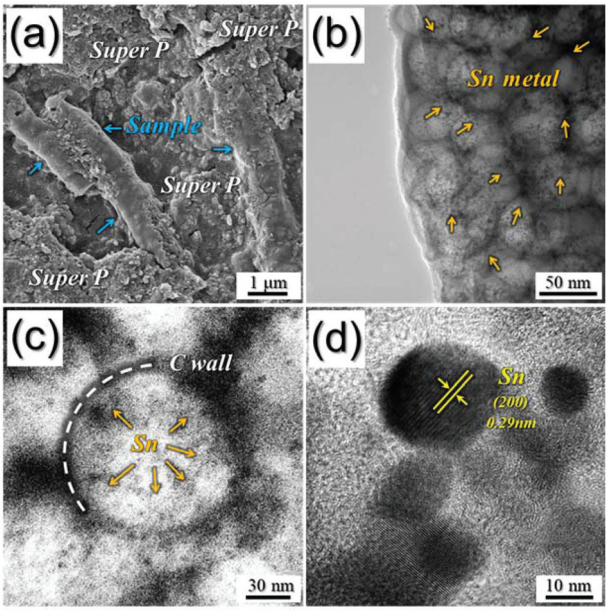

Fig. 7 (a) SEM, (b and c) TEM, and (d) HR-TEM images of RT-Sn@C porous fibers after 100 cycles.

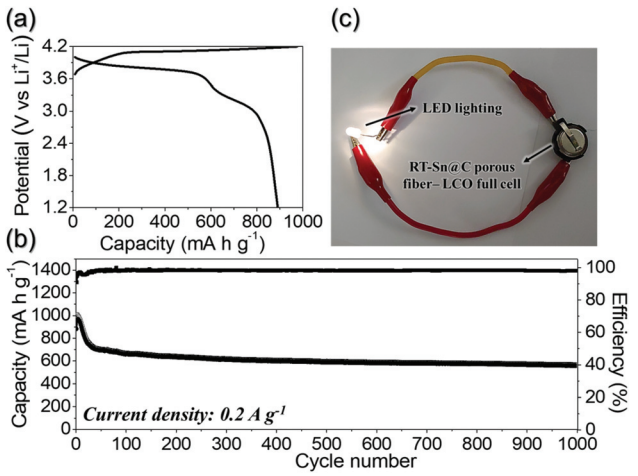

Fig. 8 Electrochemical properties of the RT-Sn@C porous fibers/$LiCoO_2$ full cell: (a) initial charge/discharge curves, (b) cycling performance, and (c) digital photographic image of a light-emitting diode lighted by the RT-Sn@C porous fibers/$LiCoO_2$ full cell.

materials can exhibit charge and discharge capacities of about 940 and 891 mA h g^{-1}, respectively, during the first cycle at a current density of 0.2 A g^{-1}, based on the mass of the RT-Sn@C porous fiber anode. As seen in Fig. 8b, the CE of the cell in the initial cycle was 91% and it increased rapidly close to an average value of 99% in the subsequent cycles. The discharge capacity and its CE of the full-cell after 1000 cycles were 557 mA h g^{-1} and approximately 100%, respectively. The RT-Sn@C porous fiber/$LiCoO_2$ powder full-cell exhibited excellent cycle performance because the numerous void spaces, each surrounding a Sn nanoparticle as a rattle-type and the surrounding carbon could accommodate the volume changes of the Sn nanoparticles during the lithiation/delithiation process efficiently. Fig. 8c presents a digital photographic image of a light-emitting diode powered by the RT-Sn@C porous fiber/$LiCoO_2$ powder full-cell.

Conclusions

In this study, we introduced for the first time the unique Sn/C composite fibers with uniformly distributed nanovoids containing one metallic Sn nanoparticle as a rattle-type, by electrospinning and a subsequent facile reduction process. The size-controlled PS nanobeads in the spinning solution enabled precise control of the void size and uniform distribution of nanovoids in the nanostructure. Therefore, reducing gas diffused efficiently into the structure through the void pathway during heat-treatment, which induced the formation of uniform sized metallic Sn nanoparticles evenly over the C matrix. Subsequently, the Sn nanoparticle was included as a rattle-type in the void space surrounded by C walls by tuning the ramping rate during heat-treatment. The unique RT-Sn@C porous fiber exhibited superior Li-ion storage properties to the composite with C fibers and separated metallic Sn nanoparticles. The new design proposed in this study could be efficiently employed to the practical implementation of the highly efficient anode materials for advanced Li ion batteries.

Conflicts of interest

There are no conflicts to declare.

Acknowledgements

This work was supported by the National Research Foundation of Korea (NRF) grant funded by the Korea government (MSIP) (NRF-2018R1A4A1024691, NRF-2017M1A2A2087577, and NRF-2018R1D1A3B07042514).

References

1 H. Liu, H.-M. Cho, Y. S. Meng and Q. Li, *ACS Appl. Mater. Interfaces*, 2014, **6**, 9842–9849.
2 M.-S. Balogun, W. Qiu, Y. Luo, H. Meng, W. Mai, A. Onasanya, T. K. Olaniyi and Y. Tong, *Nano Res.*, 2016, **9**, 2823–2851.
3 S. H. Oh, J.-S. Park, M. S. Jo, Y. C. Kang and J. S. Cho, *Chem. Eng. J.*, 2018, **347**, 889–899.
4 Z. Cai, L. Xu, M. Yan, C. Han, L. He, K. M. Hercule, C. Niu, Z. Yuan, W. Xu, L. Qe, K. Zhao and L. Mai, *Nano Lett.*, 2015, **15**, 738–744.
5 Q. Wei, F. Xiong, S. Tan, L. Huang, E. H. Lan, B. Dunn and L. Mai, *Adv. Mater.*, 2017, **29**, 1602300.

6 J. S. Cho, Y. J. Hong and Y. C. Kang, *ACS Nano*, 2015, **9**, 4026–4035.
7 J. Liu, S. Z. Qiao, J. S. Chen, X. W. D. Lou, X. Xing and G. Q. M. Lu, *Chem. Commun.*, 2011, **47**, 12578–12591.
8 M.-S. Balogun, W. Qiu, W. Wang, P. Fang, X. Lu and Y. Tong, *J. Mater. Chem. A*, 2015, **3**, 1364–1387.
9 Y. Luo, D. Yuan, M. S. Balogun, H. Yang, W. Qiu, J. Liu, P. Liu and Y. Tong, *J. Mater. Chem. A*, 2016, **4**, 13431–13438.
10 X. Huang, G. Diao, S. Li, M. S. Balogun, N. Li, Y. Huang, Z. Q. Liu and Y. Tong, *RSC Adv.*, 2018, **8**, 17056–17059.
11 C. Wu, Y. Jiang, P. Kopold, P. A. van Aken, J. Maier and Y. Yu, *Adv. Mater.*, 2016, **28**, 7276–7283.
12 R. A. Huggins, *J. Power Sources*, 1999, **81**, 13–19.
13 L. Ji, Z. Lin, M. Alcoutlabi and X. Zhang, *Energy Environ. Sci.*, 2011, **4**, 2682–2699.
14 J. R. Szczech and S. Jin, *Energy Environ. Sci.*, 2011, **4**, 56–72.
15 X. Zhou, L. J. Wan and Y. G. Guo, *Small*, 2013, **9**, 2684–2688.
16 G. Derrien, J. Hassoun, S. Panero and B. Scrosati, *Adv. Mater.*, 2007, **19**, 2336–2340.
17 H. S. Im, Y. J. Cho, Y. R. Lim, C. S. Jung, D. M. Jang, J. Park, F. Shojaei and H. S. Kang, *ACS Nano*, 2013, **7**, 11103–11111.
18 M. Noh, Y. Kwon, H. Lee, J. Cho, Y. Kim and M. G. Kim, *Chem. Mater.*, 2005, **17**, 1926–1929.
19 Y. J. Hong and Y. C. Kang, *Small*, 2015, **11**, 2157–2163.
20 C. Zhu, Y. Wen, P. A. van Aken, J. Maier and Y. Yu, *Adv. Funct. Mater.*, 2015, **25**, 2335–2342.
21 B. Luo, B. Wang, M. Liang, J. Ning, X. Li and L. Zhi, *Adv. Mater.*, 2012, **24**, 1405–1409.
22 Y. Huang, H. Liu, Y.-C. Lu, Y. Hou and Q. Li, *J. Power Sources*, 2015, **284**, 236–244.
23 L. Xia, S. Wang, G. Liu, L. Ding, D. Li, H. Wang and S. Z. Qiao, *Small*, 2016, **12**, 853–859.
24 G. Wang, H. Liu, J. Liu, S. Z. Qiao, G. M. Lu, P. Munroe and H. Ahn, *Adv. Mater.*, 2010, **22**, 4944–4948.
25 Y. Xu, Q. Liu, Y. Zhu, Y. Liu, A. Langrock, M. R. Zachariah and C. Wang, *Nano Lett.*, 2013, **13**, 470–474.
26 Y. Yu, L. Gu, C. Wang, A. Dhanabalan, P. A. van Aken and J. Maier, *Angew. Chem., Int. Ed.*, 2009, **48**, 6485–6489.
27 J. Qin, C. He, N. Zhao, Z. Wang, C. Shi, E.-Z. Liu and J. Li, *ACS Nano*, 2014, **8**, 1728–1738.
28 X. Huang, S. Cui, J. Chang, P. B. Hallac, C. R. Fell, Y. Luo, B. Metz, J. Jiang, P. T. Hurley and J. Chen, *Angew. Chem., Int. Ed.*, 2015, **54**, 1490–1493.
29 G. Wang, J.-H. Ahn, M. Lindsay, L. Sun, D. Bradhurst, S. Dou and H. Liu, *J. Power Sources*, 2001, **97**, 211–215.
30 Z. Zhu, S. Wang, J. Du, Q. Jin, T. Zhang, F. Cheng and J. Chen, *Nano Lett.*, 2013, **14**, 153–157.
31 U. K. Fatema, A. J. Uddin, K. Uemura and Y. Gotoh, *Text. Res. J.*, 2011, **81**, 659–672.
32 C. R. Martins, G. Ruggeri and M.-A. De Paoli, *J. Braz. Chem. Soc.*, 2003, **14**, 797–802.
33 S. Li, X. Zhong, Y. Song, X. Shen, J. Sun, Y. Song, R. Wang, M. Zhu, H. Zhong and A. Zheng, *J. Mater. Chem. C*, 2014, **2**, 7687–7694.
34 J. S. Cho, H. S. Ju and Y. C. Kang, *Sci. Rep.*, 2016, **6**, 23915.
35 J. Frydrych, L. Machala, J. Tucek, K. Siskova, J. Filip, J. Pechousek, K. Safarova, M. Vondracek, J. H. Seo and O. Schneeweiss, *J. Mater. Chem.*, 2012, **22**, 23232–23239.
36 H. Ma, K. Teng, Y. Fu, Y. Song, Y. Wang and X. Dong, *Energy Environ. Sci.*, 2011, **4**, 3067–3074.
37 F. Xiao, S. Yang, Z. Zhang, H. Liu, J. Xiao, L. Wan, J. Luo, S. Wang and Y. Liu, *Sci. Rep.*, 2015, **5**, 9359.
38 J. C. Groen, L. A. Peffer and J. Pérez-Ramírez, *Microporous Mesoporous Mater.*, 2003, **60**, 1–17.
39 X. Li, Y. Zhong, M. Cai, M. P. Balogh, D. Wang, Y. Zhang, R. Li and X. Sun, *Electrochim. Acta*, 2013, **89**, 387–393.
40 B. Luo, T. Qiu, D. Ye, L. Wang and L. Zhi, *Nano Energy*, 2016, **22**, 232–240.
41 M. Marcinek, L. Hardwick, T. Richardson, X. Song and R. Kostecki, *J. Power Sources*, 2007, **173**, 965–971.
42 D. Wang, X. Li, J. Yang, J. Wang, D. Geng, R. Li, M. Cai, T.-K. Sham and X. Sun, *Phys. Chem. Chem. Phys.*, 2013, **15**, 3535–3542.
43 G. Wang, J. Yao, H. Liu, S. Dou and J.-H. Ahn, *Electrochim. Acta*, 2004, **50**, 517–522.
44 X. Zhou, J. Bao, Z. Dai and Y.-G. Guo, *J. Phys. Chem. C*, 2013, **117**, 25367–25373.
45 Y. Xu, Y. Zhu, Y. Liu and C. Wang, *Adv. Energy Mater.*, 2013, **3**, 128–133.
46 S. H. Choi and Y. C. Kang, *Nanoscale*, 2015, **7**, 6230–6237.
47 Y. J. Hong, J.-K. Lee and Y. C. Kang, *J. Mater. Chem. A*, 2017, **5**, 988–995.
48 J. S. Cho, J.-S. Park, K. M. Jeon and Y. C. Kang, *J. Mater. Chem. A*, 2017, **5**, 10632–10639.
49 J.-S. Park, S. Y. Jeong, K. M. Jeon, Y. C. Kang and J. S. Cho, *Chem. Eng. J.*, 2018, **339**, 97–107.
50 H. Liu, Y. Meng and Q. Li, *RSC Adv.*, 2013, **3**, 11586–11593.